



# High efficiency solar chemical conversion using electrochemically disordered titania nanotube arrays transplanted onto transparent conductive oxide electrodes



Hye Won Jeong<sup>a</sup>, Kyu Jun Park<sup>a</sup>, Dong Suk Han<sup>b</sup>, Hyunwoong Park<sup>a,\*</sup>

<sup>a</sup> School of Energy Engineering, Kyungpook National University, Daegu 41566, Republic of Korea

<sup>b</sup> Chemical Engineering Program, Texas A&M University at Qatar, Education City, P.O. Box 23874, Doha, Qatar

## ARTICLE INFO

### Keywords:

Solar fuels  
Artificial photosynthesis  
Photoanode  
Hydrogen  
Charge transfer

## ABSTRACT

Free-standing, one-dimensional  $\text{TiO}_2$  nanotube arrays (TNAs) with a disordered surface structure are synthesized on transparent conducting substrates, and their opto-physicochemical properties and photoelectrocatalytic (PEC) performances are examined in detail. A two-step anodization process is used to transplant TNAs grown on titanium foils onto fluorine-doped  $\text{SnO}_2$  substrates (denoted as W-TNAs), after which they are electrochemically reduced for 20 and 90 s (denoted as B-TNAs-20 and 90, respectively). The as-transplanted W-TNAs exhibit low PEC activities in terms of their photocurrent, oxygen evolution reaction (OER), and oxidations of inorganic and organic substrates (iodide and urea, respectively) under simulated sunlight (AM 1.5;  $100 \text{ mW cm}^{-2}$ ), primarily because of the sluggish charge transfer through the poor electrically conductive TNA framework. The quick electrochemical reduction of the W-TNAs leads to an 8-fold larger photocurrent, while significantly accelerating the OER (by three times) and iodide and urea oxidation reactions (by 2 and  $\sim 20$  times, respectively). These enhanced PEC activities of the B-TNAs are attributed to the creation of  $\text{Ti}^{3+}$  and associated oxygen vacancies which strengthen their n-type characteristics and thereby increase their electrical conductivity. The time-resolved photoluminescence spectra further reveal that the lifetime ( $\tau$ ) of the photogenerated charge carriers in the B-TNAs ( $\tau = 0.33 \text{ ns}$ ) is an order of magnitude shorter than that of the W-TNAs ( $\tau = 3.63 \text{ ns}$ ). The disordered surface exhibits a lower Faradaic efficiency for multi-electron transfer oxidation reactions and a higher Faradaic efficiency for single-electron transfer oxidation reactions compared to the W-TNAs. The detailed surface characterization and PEC mechanism are discussed.

## 1. Introduction

The sunlight-driven photoelectrocatalytic (PEC) production of chemical fuels (e.g.,  $\text{H}_2$  via water splitting and formate via  $\text{CO}_2$  reduction) has remained a great challenge over the past four decades [1–3]. One-dimensional tubular titania nanostructures have been extensively studied as a nano-photoreactor for solar conversion because of their enlarged surface area and unique porous configuration. The electrochemical anodization of titanium (Ti) substrates in fluoride-containing solutions grows well-ordered  $\text{TiO}_2$  nanotube arrays (TNAs) on the substrates, where their length and diameter can be tailored as a function of the anodization time and electrical power (voltage and current). The as-synthesized TNAs are highly active for photocatalytic water treatment and PEC fuel production [4,5]. Furthermore, they can accommodate ions (e.g.,  $\text{Li}^+$ ) and inorganic guests (e.g.,  $\text{WO}_3$ ,  $\text{Fe}_2\text{O}_3$ ,  $\text{SrTiO}_3$ ,  $\text{CdS}$ ) [4,6,7], which widens their applicability.

Despite these advantages and potentials, TNAs still face several challenges. Technically, the TNAs grown on Ti substrates are difficult to immediately utilize in the electrode pairs (e.g., an anode–cathode couple) of stand-alone solar devices because of the non-transparent substrate. Thus, there is no choice but to irradiate TNAs through the coupled counter electrode and electrolyte. In this situation, the counter electrode and electrolyte solution must be very transparent to a broad sunlight spectrum to avoid the light-screening effect. Unfortunately, maintaining this transparency requires an expensive fabrication process and a high-quality solution [8,9]. Furthermore, the PEC performances of TNAs often vary significantly depending on the irradiation direction (substrate side vs. electrolyte side) because of the intrinsic and extrinsic properties of bare and modified TNAs. Considering larger electron mobility due to a lower effective mass compared to photogenerated holes, the irradiation of the electrolyte side is expected to lead to a higher PEC efficiency with a given thick film [10]; however, this does

\* Corresponding author.

E-mail address: [hwp@knu.ac.kr](mailto:hwp@knu.ac.kr) (H. Park).

not always occur [11–13].

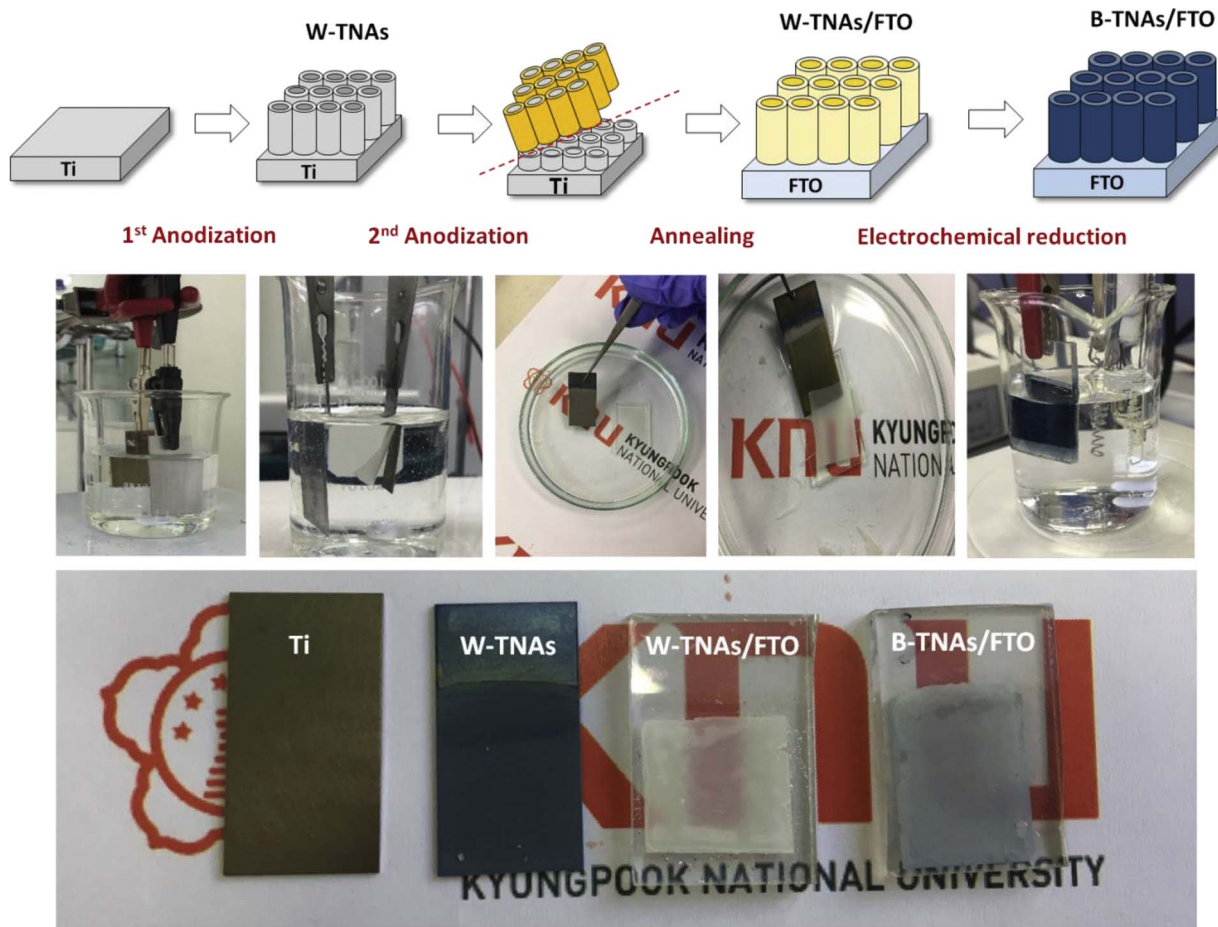
An increase in the tube length of aligned TNAs should be beneficial in absorption, leading to a high efficiency. However, the PEC efficiency does not necessarily increase with the tube length because of a trade-off between the absorption and the charge carrier diffusion. With an increase in the tube length, the photogenerated electrons must travel a longer distance, and a significant fraction of the electrons recombine with holes when they arrive at the Ti substrate. The most widely employed method to enhance the charge transfer is to increase the electrical conductivity of the  $\text{TiO}_2$  by intercalating metals (Bi, Nb, Li, etc.) [14–16] and non-metals (C, N, S, H, etc.) [17]. In particular, the treatment of  $\text{TiO}_2$  in a reductive environment leads to blue-colored  $\text{TiO}_2$ , which displays a higher electrical conductivity than pristine, white  $\text{TiO}_2$  [18–20]. With this in mind, we attempted to synthesize free standing blue TNAs (B-TNAs) on transparent conducting oxide (TCO) substrates via the two-step anodization of Ti substrates. For the synthesis of B-TNAs, the first anodization step was used to grow amorphous TNAs. Annealing these produced crystalline white TNAs (W-TNAs), as well as an oxide barrier layer in the TNA/Ti interface. In the second anodization step, the W-TNAs were peeled off of the Ti substrates and transferred to TCO substrates. These free-standing W-TNA/TCO samples were electrochemically reduced in a phosphate buffer solution, forming blackish TNAs (denoted as B-TNAs) (Scheme 1). The B-TNAs were expected to generate large photocurrents because of their enhanced absorption and facilitated charge transfer [19,20]. Various surface analyses were performed to examine their morphology and material property changes, and understand the charge transfer phenomena.

## 2. Experimental section

### 2.1. Synthesis of TNAs on transparent glass substrate

All of the analytical grade reagents and chemicals were purchased from Sigma-Aldrich and used without further purification, unless otherwise mentioned. TNAs were fabricated on transparent conducting oxide substrates via two-step anodization [21]. Titanium foil (0.5 mm thick, 99%, Alfa Aesar) was polished with sandpaper (AA400) and cleaned using ultrasound in ethanol, acetone, and deionized water ( $> 18 \text{ M}\Omega \text{ cm}$ ) for 10 min, followed by drying in an  $\text{N}_2$  gas stream. The as-prepared Ti foils were electrochemically anodized in an ethylene glycol solution (99%, Daejung) containing ammonium fluoride (0.15 M) and deionized water (2 vol%) using a DC voltage of 50 V for 3 h. Then, the specimens were washed with ethanol, and annealed sequentially at 200 °C for 30 min and 480 °C for 1 h to crystallize the TNAs on the Ti foil (TNA/Ti). In the second step, the as-synthesized TNA/Ti samples were anodized again at a DC voltage of 60 V until a film of TNAs peeled off of the Ti foil (Scheme 1). The free-standing TNA samples were then carefully collected and dried under ambient conditions.

Fluorine-doped  $\text{SnO}_2$  substrates (FTO, ~500 nm thick, 2 cm × 2 cm, 8  $\Omega/\text{square}$ , Pilkington Co., Ltd.) were washed with ethanol and deionized water. Then, a titanium precursor solution was prepared by mixing 2-propanol (99.5%, Duksan), titanium tetrakisopropoxide (98%, Junsei), Triton X-100, and acetic acid at the volume ratio of 1:10:4:2. This precursor solution was dropped onto the FTO and spread using a spin-coating system at 3000 rpm for 1 min, followed by annealing at 450 °C for 30 min. This coating-annealing cycle was repeated five times to obtain a buffer layer of ~400 nm on the FTO (Fig. S1). Then, the as-



**Scheme 1.** Synthetic process for blue  $\text{TiO}_2$  nanotube arrays vertically aligned onto transparent conducting oxide substrates.

synthesized TNA films were carefully placed onto the FTO while injecting 80  $\mu\text{L}$  of the precursor solution into the TNA/FTO interface. After drying under ambient conditions, the samples were annealed at 200  $^{\circ}\text{C}$  for 15 min and 480  $^{\circ}\text{C}$  for 30 min (denoted as W-TNAs). To synthesize the B-TNAs, the as-obtained W-TNA samples (working electrode), saturated calomel electrode (SCE; reference electrode), and Pt wire (counter electrode) were placed in an aqueous  $\text{KH}_2\text{PO}_4$  buffer solution (0.1 M; pH 7.2) and a constant current of  $-17 \text{ mA cm}^{-2}$  was applied to the working electrode for two different time periods (20 and 90 s) (denoted as B-TNAs-20 and B-TNAs-90, respectively).

## 2.2. Photoelectrocatalytic activity tests

The PEC performances of the TNAs were tested using a three-electrode system with the SCE (reference electrode) and Pt wire (counter electrode) in a customized glass reactor containing an aqueous sodium sulfate solution (0.1 M) at pH  $\sim 6.5$ . A 150 W Xenon arc lamp (ABET Tech., U.S.A.) equipped with an air mass (AM) 1.5 G filter was used as a light source ( $100 \text{ mW cm}^{-2}$ ). Light was irradiated on the substrate side of  $0.5 \text{ cm}^2$ . Linear sweep voltammograms (LSVs) were obtained by sweeping the potential from  $-0.5$  to  $+2.0 \text{ V}$  vs. SCE at a scan rate of  $10 \text{ mV s}^{-1}$  in the absence or presence of the irradiation. The incident photon-to-current efficiency (IPCE) was estimated using a CS-130 monochromator (Mmac-200, Spectro) with a 300 W Xe arc lamp using the following equation [22].

$$\text{IPCE}(\%) = (1239.8 \times I_{\text{ph}}) \times 100 / (P_{\text{light}} \times \lambda) \quad (1)$$

where  $I_{\text{ph}}$ ,  $P_{\text{light}}$ , and  $\lambda$  refer to the photocurrent density ( $\text{mA cm}^{-2}$ ) at  $+1 \text{ V}$  vs. SCE, photon flux ( $\text{mW cm}^{-2}$ ), and wavelength (nm), respectively. An electrochemical impedance analysis was performed in the frequency range of 100 kHz–0.1 Hz at an AC voltage of 20 mV (Ivium Compact Stat) in an aqueous sodium sulfate solution (0.1 M). To examine the doping level and flat band potential ( $E_{\text{fb}}$ ), Mott–Schottky plots were obtained in the frequency range of 10 kHz–0.01 Hz while sweeping the potential in the range of  $-1$  to  $+0.6 \text{ V}$  vs. SCE at a scan rate of  $50 \text{ mV s}^{-1}$ . The doping level and  $E_{\text{fb}}$  were estimated using the following equation [23].

$$\frac{1}{C_{\text{SC}}^2} = \frac{2}{q\epsilon\epsilon_0 N_d} \left( E - E_{\text{fb}} - \frac{kT}{q} \right) \quad (2)$$

where  $C_{\text{SC}}$ ,  $q$ ,  $\epsilon$ ,  $\epsilon_0$ ,  $N_d$ ,  $E$ ,  $k$ , and  $T$  refer to the space charge capacitance (F), elementary charge ( $1.602 \times 10^{-19} \text{ C}$ ), relative dielectric constant of  $\text{TiO}_2$  [24], permittivity of vacuum ( $8.85 \times 10^{-12} \text{ N}^{-1} \text{ C}^2 \text{ m}^{-2}$ ), donor density ( $\text{cm}^{-3}$ ), applied potential (V), Boltzmann's constant ( $1.38 \times 10^{-23} \text{ J K}^{-1}$ ), and absolute temperature (K), respectively.

The PEC activities of the as-synthesized samples were examined in terms of the oxidation of iodide ( $\text{I}^-$ , 20 mM) to triiodide ( $\text{I}_3^-$ ) in an aqueous sodium sulfate solution (0.1 M) at a constant potential of 1 V vs. SCE [25]. The produced triiodide was quantified by measuring the absorbance at  $\lambda = 352 \text{ nm}$  using a UV-vis spectrometer (Shimadzu UV-2450). The PEC decomposition of urea (1 mM, Junsei) was performed in an aqueous sodium sulfate solution (0.1 M) with 20 mM of NaCl at 1 V vs. SCE. The aliquots (0.5 mL) were intermittently sampled and analyzed using ion chromatography (Dionex ICS-1100). The urea concentration was determined by estimating the difference between the  $\text{NH}_4^+$  produced from the reaction with urease (Worthington Biochemical Corporation) and the  $\text{NH}_4^+$  present before the reaction with urease. The detailed analytical procedure can be found elsewhere [26]. In addition, the evolution of molecular oxygen ( $\text{O}_2$ ) via water oxidation was tested at a constant potential and current (1 V vs. SCE,  $0.5 \text{ mA cm}^{-2}$ ) in a 0.1 M sodium sulfate electrolyte. The headspace gas of the reactor was intermittently sampled and analyzed for  $\text{O}_2$  using a gas chromatograph (Young Lin, ACME 6100) equipped with a thermal conductivity detector and a molecular sieve 5  $\text{\AA}$  column during the PEC reaction. Before irradiation,  $\text{N}_2$  gas ( $> 99.9\%$ ) was purged through the

solution for 1 h to remove the  $\text{O}_2$  in the solution and headspace. Hereafter, the notation “vs. SCE” is omitted for simplicity unless otherwise specified.

## 2.3. Surface characterization

The morphology of the as-synthesized samples was analyzed using field-emission scanning electron microscopy (FE-SEM, Hitachi S4800). The X-ray diffraction (XRD, PANalytical Empyrean) and an X-ray photoelectron spectroscope (XPS, ULVAC-PHI 5500) equipped with an Al  $\text{K}\alpha$  monochromator were used to examine the crystallite structure and elemental states of the samples, respectively. A UV-vis spectrometer (Shimadzu UV-2450) was used to measure the transmittance [27]. Electron paramagnetic resonance (EPR) measurements were performed at the Korea Basic Science Institute (KBSI), Western Seoul center, Korea. CW X-band (9.6 GHz) EPR spectra were collected on a Bruker EMX plus 6/1 spectrometer equipped with an Oxford Instrument ESR900 liquid He cryostat using an Oxford ITC 503 temperature controller. All of the spectra were collected using the following experimental parameters: a microwave frequency of 9.6 GHz, 1 mW of microwave power, a modulation amplitude of 10 G, a time constant of 40.96 ms, 4 scans, and a temperature of 4 K. Time-resolved photoluminescence (TRPL) emission decay spectra were obtained using an inverted-type scanning confocal microscope (MicroTime-200, Picoquant, Germany) with a  $20 \times$  objective. The measurements were performed at the Korea Basic Science Institute (KBSI), Daegu Center, Korea. A single-mode pulsed diode laser (379 nm with a pulse width of  $\sim 30 \text{ ps}$  and  $\sim 5 \mu\text{W}$  of laser power) was used as an excitation source. The details of the analytical conditions were reported elsewhere [25,28–30].

## 3. Results and discussion

### 3.1. Electrochemical creation of $\text{Ti}^{3+}$ and oxygen vacancy

Fig. 1a and b shows top and cross-sectional FE-SEM images of a typical B-TNA sample, respectively, fabricated on the FTO substrate via the two-step anodization and subsequent electrochemical reduction processes. The as-synthesized B-TNA sample exhibited a vertically aligned tubular structure with a pore size of  $\sim 100 \text{ nm}$  and tube length of  $\sim 15 \mu\text{m}$ . The W-TNA samples showed a similar morphology (Fig. S2), which indicates that the employed electrochemical reduction process causes virtually no damage as a result of the short processing times (20 and 90 s). The crystalline structures of the W-TNAs and B-TNAs were further compared using XRD (Fig. 1c). The samples exhibited the same XRD pattern with the primary characteristic peaks of anatase  $\text{TiO}_2$  (e.g., (101), (004), and (200) planes at  $2\theta = 25.28^\circ$ ,  $37.80^\circ$ , and  $48.05^\circ$ , respectively; JCPDS #00-021-1272).

Although they had the same morphologies and crystalline structures, the UV-vis transmittance spectra of the W-TNA and B-TNA samples were significantly different (Fig. 1d). The former exhibited a transmittance of  $\sim 45\%$  at  $\lambda = 450 \text{ nm}$ , which decreased to  $\sim 28\%$  and  $\sim 15\%$  in the B-TNAs-20 and B-TNAs-90, respectively. Consistent with the transmittance spectra, the W-TNA sample was yellowish white, whereas the B-TNAs-20 and B-TNAs-90 were gray and blue, respectively (Fig. 1d inset). This gray-to-blue color is typically found in partially reduced  $\text{TiO}_2$  samples with oxygen vacancies (e.g.,  $\text{Ti}^{(4-x)+}\text{O}_{2-y}$ ) [31,32]. The  $\text{Ti}(\text{IV})$  reduction appeared to proceed with the electrochemical reduction time (20 and 90 s), changing the color.

Further XPS analyses of the W-TNAs and B-TNAs were performed to examine the oxidation states of the Ti and O in the samples (Fig. 2a). The  $\text{Ti}2\text{p}$  spectra of the W-TNAs showed two  $\text{Ti}(\text{IV})$ -associated bands centered at  $\sim 458.6$  (2p1/2) and  $\sim 464.3 \text{ eV}$  (2p3/2). These bands shifted by  $\sim 0.2 \text{ eV}$  to a low binding energy region in the B-TNAs-20 sample because of the partial reduction of the  $\text{Ti}(\text{IV})$  [31,33]. Interestingly, the bands in the B-TNAs-90 shifted to a high binding energy region close to that of the W-TNAs. We further compared the binding

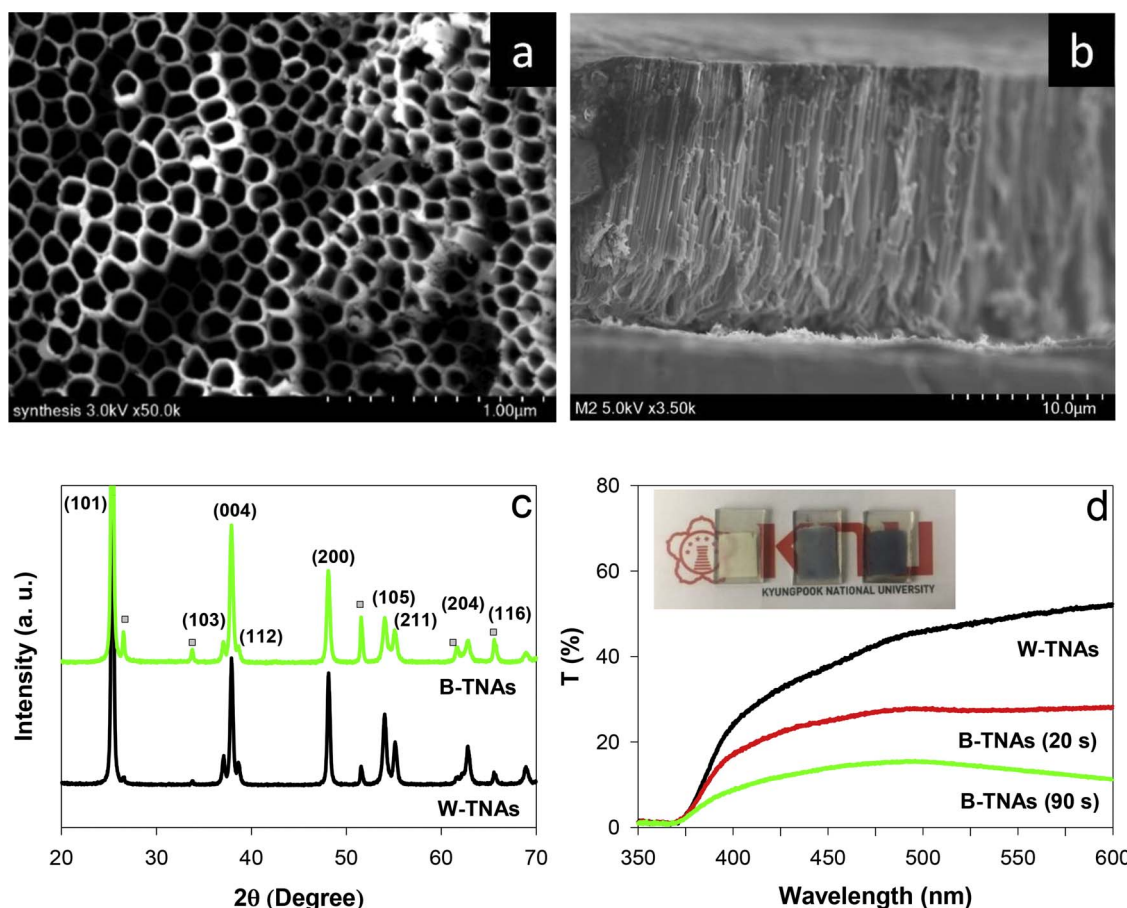


Fig. 1. (a and b) Top and cross-sectional FE-SEM images of B-TNAs (90 s), respectively, synthesized on FTO substrates. (c) XRD patterns of W- and B-TNAs (90 s) (□: FTO). (d) UV-vis transmittance spectra of W- and B-TNAs (20 and 90 s). Inset shows photos of the samples.

energy of  $\text{Ti}2\text{p}1/2$  band as a function of electrochemical reduction time (5–90 s) and found that the shift of the binding energy ( $\Delta\text{BE}$ ) was greatest in the 20 s-reduced sample and then decreased in the sample reduced for 90 s (Fig. 2a inset). This re-shift by the prolonged electrochemical reduction is rather difficult to fully understand. Actually, we found a large  $\text{H}_2$  evolution during the electrochemical reduction process, which was associated with the oxidation of the reduced  $\text{TiO}_2$  in the TNA/solution interface (e.g., mouth surface) [34]. Upon the application of the reduction current ( $-17 \text{ mA cm}^{-2}$ ), the bottom region of TNAs can be immediately reduced, and the reduction is propagated to the mouth surface via the framework ( $\sim 15 \mu\text{m}$  long). However, the electrons that arrive at the mouth surface are used for the  $\text{H}_2$  evolution. Considering the analytical depth in a typical XPS ( $\sim 10 \text{ nm}$ ), the reduced state of the mouth appeared to have been maintained for  $> 20 \text{ s}$ , and a fraction of the mouth surface ( $\sim 10 \text{ nm}$  thick) could have been oxidized when the  $\text{H}_2$  evolution began. Similarly to our result, Zhou and Zhang observed decreases in  $\Delta\text{BE}$  of the  $\text{Ti}2\text{p}$  band with increasing electrochemical reduction potentials [31], which was attributed to a competitive  $\text{H}_2$  evolution. It is noteworthy that chemical and/or electrochemical reduction treatment of  $\text{TiO}_2$  did not always accompany the shift of  $\text{Ti}2\text{p}$  band [20,35], even though the treated samples turned blue or black. This indicates that the surface Ti state of reduced  $\text{TiO}_2$  is quite sensitive to synthetic condition and analytical environment.

To gain confirmation of oxygen vacancies, the as-synthesized W-TNAs and B-TNAs were analyzed using a Raman spectrometer (Fig. 2b). The W-TNAs exhibited six characteristic peaks ( $3\text{E}_g$  modes,  $2\text{B}_1g$  modes, and an  $\text{A}_1g$  mode) of anatase  $\text{TiO}_2$ , with the strongest  $\text{E}_g$  mode at  $143.4 \text{ cm}^{-1}$ . It should be noted that the  $\text{E}_g$  mode-associated peak is sensitive to the degree of disorder (i.e., oxygen vacancy) [32], and usually shifts and broadens in the presence of oxygen vacancy-oriented

surface defects [36]. In contrast to the W-TNAs, the  $\text{E}_g$  mode peaks in the B-TNAs were shifted to  $144.5 \text{ cm}^{-1}$ , and their full width at half maximum (FWHM) value increased from  $13 \text{ cm}^{-1}$  to  $13.6 \text{ cm}^{-1}$  (Fig. 2b inset). This indicates that the level of oxygen vacancies (i.e., the degree of disorder) increased with the electrochemical reduction. To estimate the oxygen vacancies, the XPS O1s band spectra were deconvoluted into the lattice oxygen ( $\text{Ti}-\text{O}-\text{Ti}$ ) centered at  $529.7 \text{ eV}$  and the surface oxygen ( $> \text{Ti}-\text{O}-\text{H}$ ) centered at  $531 \text{ eV}$ . The states of the latter were reported to be associated with the oxygen vacancies [19,20] and hence their fractions with respect to the total oxygen were quantified. As shown in Fig. 2a inset, the fraction of surface oxygen increased from  $\sim 15\%$  (W-TNAs) to  $\sim 27\%$  (B-TNAs-90) (Fig. S3), which was consistent to the Raman analysis.

The reduction of  $\text{Ti}(\text{IV})$  in the W-TNA samples through the electrochemical reduction was further examined using the EPR spectrometer at  $4 \text{ K}$  (Fig. 2c). The W-TNAs showed a  $g$ -value of  $2.025$ , which corresponded to the  $\text{Ti}^{4+}-\text{O}^{2-}$  in anatase  $\text{TiO}_2$  [37]. Similar  $g$ -values were observed for the B-TNA samples. On the other hand, two new  $g$ -values at  $1.968$  and  $1.949$  were found for the B-TNAs-20 and B-TNAs-90 [38], respectively, while the  $g$ -value became gradually stronger with an increase in the electrochemical reduction time (0, 20, and 90 s) [39]. Considering that a  $g$ -value of less than two is typically associated with the lattice  $\text{Ti}^{3+}$  [40], the B-TNA samples should contain a fraction of  $\text{Ti}^{3+}$  states. The trapped electrons (i.e.,  $\text{Ti}^{3+}$ ) and/or resultant oxygen vacancies could work as trap sites below the conduction band, leading to an extended absorption from the UV to visible region (i.e., a color change from white to blue) [41].

Mott–Schottky plots of the W-TNAs and B-TNAs were obtained to gain insight into the donor-doping levels and flatband potentials ( $E_{\text{fb}}$ ) (Fig. 2d). The slope (proportional to  $N_D^{-1}$ , see Eq. (2)) of the B-TNAs

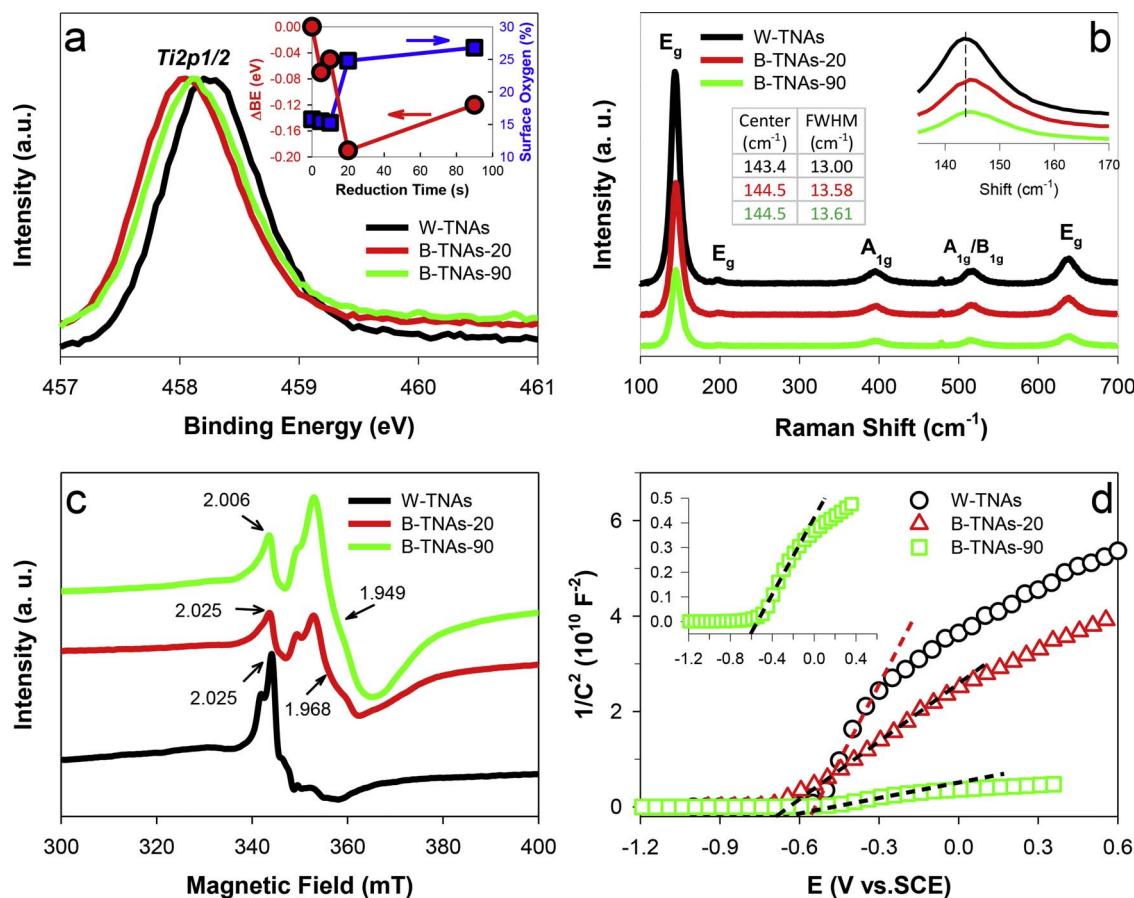


**Fig. 2.** (a) Ti2p XPS spectra (inset: the binding energy shift of Ti2p1/2 band and the fraction of surface oxygen as a function of electrochemical reduction time), (b) Raman spectra (insets: magnified spectra and tables for Raman shifts and FWHM values of strongest  $E_g$  modes), (c) EPR spectra recorded at 4 K, and (d) Mott-Schottky plots of W-TNAs and B-TNAs.

90 ( $N_D = 5.73 \times 10^{22} \text{ cm}^{-3}$ ) was estimated to be the smallest followed by that of the B-TNAs-20 ( $N_D = 1.12 \times 10^{22} \text{ cm}^{-3}$ ) and W-TNAs ( $N_D = 3.55 \times 10^{21} \text{ cm}^{-3}$ ) (Table S1). Although there was no extrinsic high valent-donor (e.g.,  $\text{Nb}^{5+}$  and  $\text{Sb}^{5+}$ ) to induce  $\text{Ti}^{3+}$  for an overall charge neutrality (e.g.,  $\text{Ti}^{4+}$ - $\text{Nb}^{5+}$ - $\text{Ti}^{3+}$ ), an increase in the  $N_D$  simply by the electrochemical reduction was attributed to the creation of oxygen vacancies leading to the formation of  $\text{Ti}^{3+}$  [31]. The presence of the reduced states can increase the n-type characteristic and shift the flatband potential in the negative potential direction. In accordance with this speculation, the flatband potentials of the W-TNAs, B-TNAs-20, and B-TNAs-90 were estimated to be  $-0.53$ ,  $-0.64$ , and  $-0.60 \text{ V}$ , respectively (Table S1). A negative shift in  $E_{fb}$  should induce a larger band-bending, enhancing the charge separation. The non-linear shift of  $E_{fb}$  with the electrochemical reduction time could be attributed to the porous structure with a non-uniform surface [22]. The impedance analysis further revealed two-orders-of-magnitude decreases in the charge transfer resistances at the TNA/solution interface and within the TNA bulk by the electrochemical reduction (Fig. S4 and Table S1). This indicates that the formation of  $\text{Ti}^{3+}$  and oxygen vacancies increased the electrical conductivity and facilitated the charge transfer. A similar effect can be found with the doping of high-valence donors [42].

### 3.2. Photoelectrochemical behaviors of W-TNAs and B-TNAs

The photoelectrochemical behaviors of the W-TNA and B-TNA samples were compared in a 0.1 M sodium sulfate solution ( $\text{pH} \sim 6.5$ ) under AM 1.5 light ( $100 \text{ mW cm}^{-2}$ ) (Fig. 3a). The W-TNAs exhibited a photocurrent onset potential ( $E_{on}$ ) at approximately  $-0.5 \text{ V}$  and a photocurrent plateau of  $\sim 0.3 \text{ mA cm}^{-2}$  at  $\sim 0 \text{ V}$ . The maintenance of a plateau to  $E \sim 1.5 \text{ V}$  that is sufficient for large band-bending indicates

that the charge transfer in the W-TNAs was very sluggish. A dramatic increase in the photocurrent from  $\sim 1.6 \text{ V}$  was attributed to the overlapping of the Fermi level ( $E_F$ ) and valence band edge ( $E^{\circ} \text{ VB}$ ) (i.e., dark current generation). The B-TNA samples showed a value of  $E_{on}$  that was similar to that of the W-TNAs, and yet they had significantly larger photocurrents (e.g.,  $0.71$  and  $0.85 \text{ mA cm}^{-2}$  at  $0.6 \text{ V}$  for B-TNAs-20 and B-TNAs-90, respectively). At a constant potential of  $0 \text{ V}$ , however, the B-TNAs underwent photocurrent decreases over time, whereas the photocurrent of the W-TNAs was nearly constant (Fig. 3a inset). This indicates that a significant fraction of the charge carriers underwent recombination in the B-TNAs at  $0 \text{ V}$ . However, the photocurrent transients nearly vanished at  $1 \text{ V}$  as a result of sufficient band-bending (see Fig. 3b inset). The IPCE profiles of the W- and B-TNAs were further compared at  $1 \text{ V}$  (Fig. 3b). The W-TNAs showed an IPCE of  $\sim 5\%$  at  $\lambda = 380 \text{ nm}$ , which was increased by three and six times in the B-TNAs-20 and B-TNAs-90, respectively. However, although the B-TNA samples absorbed visible light ( $\lambda > 420 \text{ nm}$ , see Fig. 1d), they did not generate photocurrents in the wavelength range of visible light.

The enhanced PEC performance of the B-TNA samples could be attributed to the reduced charge transfer resistance resulting from the creation of  $\text{Ti}^{3+}$  and oxygen vacancies (Figs. 2d and S3). To gain insights into the charge transfer kinetics, the time-resolved photoluminescence (TRPL) emission (green emission,  $\lambda > 500 \text{ nm}$ ) decay spectra of the W-TNAs and B-TNAs (excited at  $\lambda = 375 \text{ nm}$ ) were compared (Fig. 4, see Fig. S5 for the blue-emission at  $\lambda = 405 \text{ nm}$ ). It was evident that the B-TNAs exhibited a PL decay (average  $\tau = 0.33 \text{ ns}$ ) that was an order of magnitude faster than that of the W-TNAs (average  $\tau = 3.63 \text{ ns}$ ). The comparison between the W-TNAs and B-TNAs-90 further revealed that the latter provided rapid charge transfer pathways, presumably via the  $\text{Ti}^{3+}$ -associated trap sites (coordinated to

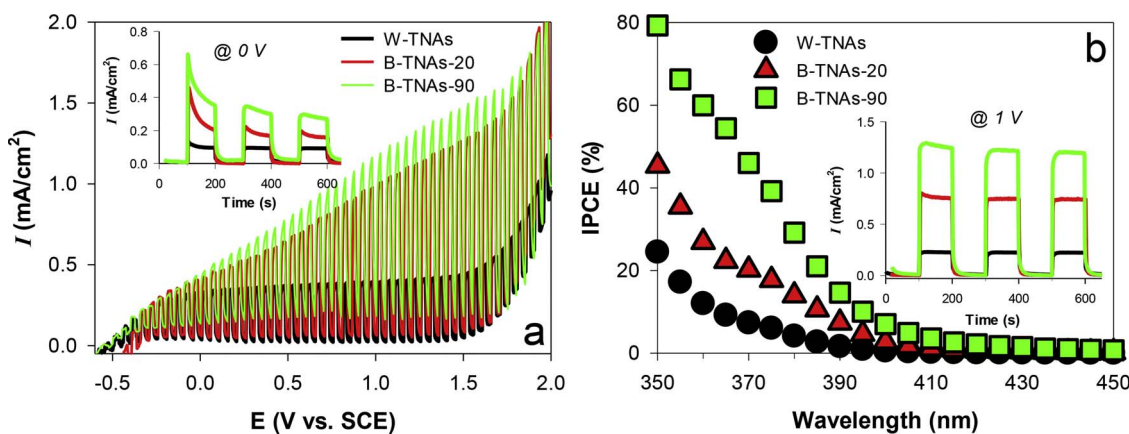


Fig. 3. (a) Light-chopped linear sweep voltammograms of W-TNAs and B-TNAs in aqueous sodium sulfate (0.1 M) under simulated sunlight (AM 1.5, 100 mW cm<sup>-2</sup>). Inset shows the light-chopped photocurrent profiles at 0 V vs. SCE. (b) IPCE profiles of W-TNAs and B-TNAs as function of irradiation wavelength in aqueous sodium sulfate (0.1 M) at 1 V vs. SCE. Inset shows the light-chopped photocurrent profiles at 1 V vs. SCE.

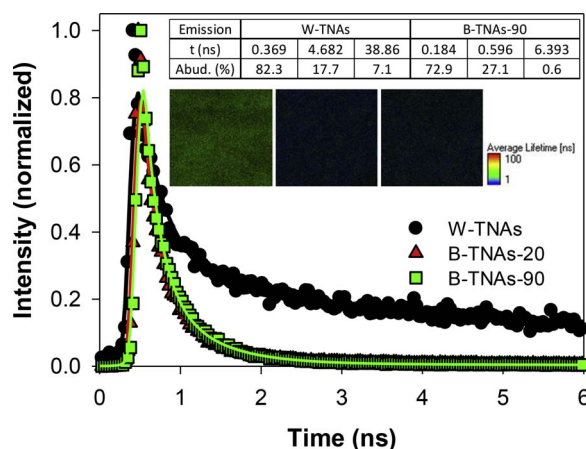


Fig. 4. Time-resolved photoluminescence (TRPL) emission ( $\lambda > 500$  nm) decay spectra of samples (excited at  $\lambda = 375$  nm). Inset shows the lifetimes of charge carriers in the samples. Two-dimensional PL lifetime images of the samples are also shown (from left: W-TNAs, B-TNAs-20, and B-TNAs-90).

electrochemically inserted protons). The B-TNAs-20 showed similar yet slightly delayed decay kinetics compared to the B-TNAs-90 (Table S1). These charge transfer kinetics were uniformly found over the entire samples, which were compared using PL 2D images (Fig. 4 inset), indicating the uniform distribution of the trap sites.

### 3.3. Photoelectrocatalytic performances of W-TNAs and B-TNAs

The photoelectrocatalytic performances of the W-TNAs and B-TNAs were examined for the oxygen evolution reaction (OER) via water oxidation (R1).



As shown in Fig. 5a and b, the W-TNAs produced  $\text{O}_2$  at a rate of  $\sim 1 \mu\text{mol h}^{-1}$ , with a Faradaic efficiency of  $\sim 95\%$  (Fig. S6). Considering the absence of OER catalysts (e.g.,  $\text{IrO}_x$ ,  $\text{CoO}_x$ ,  $\text{NiO}_x$ ) [43–45], this Faradaic efficiency was remarkably high. The  $\text{O}_2$  production rate of the B-TNAs-20 was enhanced to  $\sim 2.5 \mu\text{mol h}^{-1}$ ; however, the Faradaic efficiency was noticeably decreased to  $\sim 75\%$ . The OER was further enhanced with the B-TNAs-90 ( $\sim 3 \mu\text{mol h}^{-1}$ ), and the Faradaic efficiency was reduced to  $\sim 50\%$ . Similar results were obtained when constant currents ( $0.5 \text{ mA cm}^{-2}$ ) were applied to the W-TNAs and B-TNAs (Fig. S7). Considering that the surface defects (i.e., oxygen vacancies) are essential for the dissociative adsorption of water [46], the reduced Faradaic efficiencies with the B-TNAs samples were contrary to

expectation. There are several possible reasons. First of all, the surface states of B-TNAs can change under irradiation. We have found that positive potential-biased B-TNAs samples were slightly bleached after PEC tests, indicating that the reduced states of  $\text{TiO}_2$  (i.e.,  $\text{Ti}^{(4-x)+}\text{O}_{2-y}$ ) vanished. This PEC-induced oxidation of  $\text{TiO}_2$  can diminish the role of the oxygen vacancies in the OER process. Furthermore, increases in the level of oxygen vacancies by the electrochemical reduction process were relatively insignificant (e.g., 15% to 27% as shown in Fig. 2a inset), less contributing to the OER. Second,  $\text{O}_2$  adsorption can be more favorable than  $\text{H}_2\text{O}$  adsorption particularly at the defect sites where electron density is high enough to create bonds between the surface and  $\text{O}_2$  [47]. In this case, even if the OER proceeds, the actual amount of  $\text{O}_2$  gas accumulated in a reactor headspace can be smaller than that produced via water splitting. Finally, multi-electron water oxidations can be shifted into single-electron water oxidations. The dissociative water adsorption leads to production of two adsorbed hydroxides ( $\text{OH}^-$ ) [46], which can be transformed into surface-bound hydroxyl radicals ( $\text{OH}^\cdot$ ) (*vide infra*).

The photoelectrocatalytic performances of the TNAs were further compared for the oxidation of iodide ( $\text{I}^-$ ) as an alternative substrate, which is transformed to triiodide ( $\text{I}_3^-$ ) via single-electron transfers (R2)–(R5).



In contrast to the OER results, the B-TNAs-90 exhibited the highest production of triiodide, followed by the B-TNAs-20 and W-TNAs (Fig. 5c and d). The Faradaic efficiencies with the B-TNAs-90 and B-TNAs-20 at 30 min were 70% and 50%, respectively, whereas the W-TNAs showed a reduced Faradaic efficiency of 40%. The gradual decrease in the triiodide production rate was attributed to the electrochemical reductions of diiodide and triiodide at the counter electrode, leading to the overall low Faradaic efficiency. The comparison between the water oxidation and iodide oxidation indicates that the  $\text{Ti}^{3+}$  creation played a positive role, particularly in single-electron transfer reactions. For effective multi-electron transfers, substrate molecules ( $\text{H}_2\text{O}$  in this study) need to adsorb on the surface with suitable adsorption energy. The creation of  $\text{Ti}^{3+}$  and oxygen vacancies appeared to disorder the  $\text{TiO}_2$  surface and affect the adsorption states of  $\text{H}_2\text{O}$ .

To maximize the single-electron transfer phenomena, chloride (20 mM) was added to the sulfate electrolyte (0.1 M), and the PEC decomposition of urea was conducted using the W-TNAs and B-TNAs-90

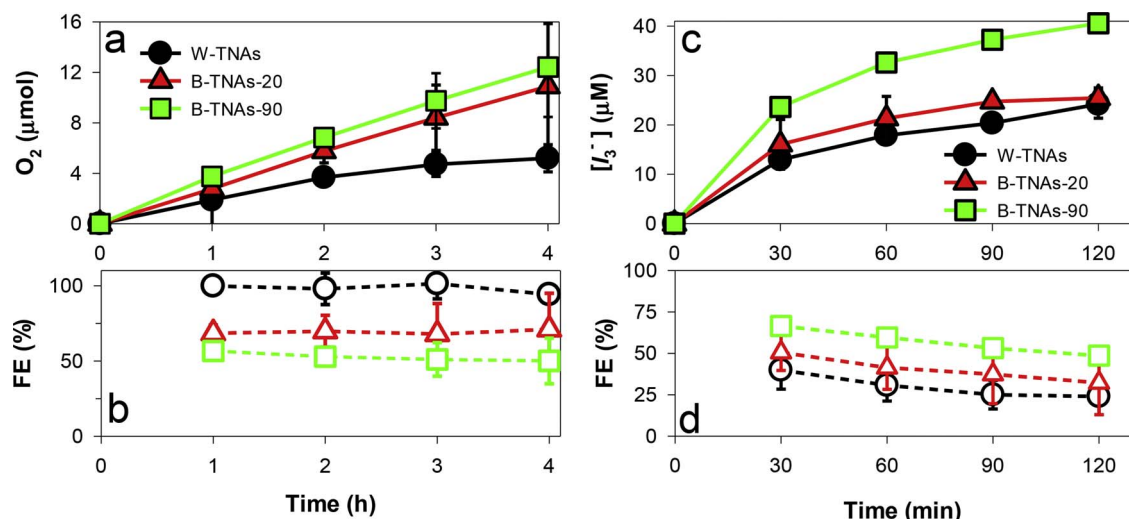


Fig. 5. Photoelectrocatalytic comparison of W-TNAs and B-TNAs at 1 V vs. SCE for (a and b) water oxidation (a: oxygen evolution, b: Faradaic efficiency) and (c and d) iodide oxidation (c: triiodide production, d: Faradaic efficiency) under simulated sunlight (AM 1.5, 100 mW cm<sup>-2</sup>). Electrolyte: 0.1 M sodium sulfate.

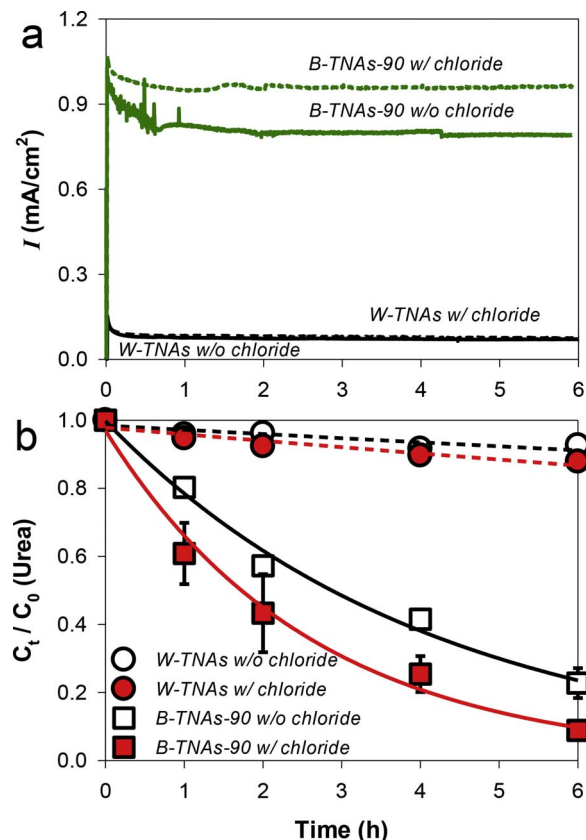
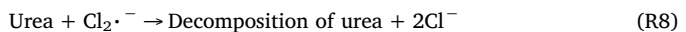
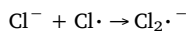
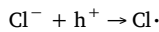


Fig. 6. Photoelectrocatalytic decomposition of urea in aqueous sodium sulfate electrolyte (0.1 M) without (w/o) and with (w/) chloride using W-TNAs and B-TNAs-90 at 1 V vs. SCE.  $[Urea]_0 = 1 \text{ mM}$ ,  $[Cl^-] = 20 \text{ mM}$ .

(Fig. 6). The W-TNAs produced a photocurrent of  $0.1 \text{ mA cm}^{-2}$  in the sulfate electrolyte, and the addition of chloride did not cause any change in the photocurrent (Fig. 6a). In accordance with the photocurrent results, the urea concentration with the W-TNAs insignificantly changed over time in the absence and presence of chloride (Fig. 6b). This confirmed that the transplanted W-TNAs were not active in the generation of either OH radicals via one-electron water oxidation (R2) or reactive chlorine species (RCS) via the one-electron oxidation of chloride (R6) and (R7)).



In contrast, when using the B-TNAs-90, the addition of chloride enhanced the photocurrent from  $\sim 0.8$  to  $1.0 \text{ mA cm}^{-2}$ , accelerating the decomposition of urea. Assuming the pseudo-first order reaction ( $C_t = C_0 \exp(-kt)$ , where  $k$  and  $t$  refer to the rate constant ( $\text{h}^{-1}$ ) and time (h), respectively), the rate constants for the urea decomposition were estimated to be  $0.24$  and  $0.39 \text{ h}^{-1}$ , in the absence and presence of chloride, respectively. This strongly confirmed the pathway for the RCS-mediated decomposition of urea, as often observed with electrocatalytic processes in chloride electrolytes [14,26,48,49]. It should be noted that the rate constants with the B-TNAs-90 were an order of magnitude greater than those with the W-TNAs ( $0.013$  and  $0.020 \text{ h}^{-1}$  in the absence and presence of chloride, respectively).

#### 4. Conclusions

$TiO_2$  nanotube arrays grown on titanium foils via an electrochemical anodization process were successfully transplanted onto transparent conducting substrates. The as-synthesized, white TNA samples were demonstrated to possess PEC activities in terms of photocurrent generation and the oxidation of water and aquatic substrates. Nevertheless, the PEC activities were still limited, primarily owing to the sluggish charge transfer associated with low electrical conductivity. The electrochemical reduction process employed for the W-TNAs was found to be effective in enhancing the electrical conductivity and thereby accelerating the charge transfer by a factor of 10. The optimized sample (i.e., B-TNAs-90) produced an  $\sim 8$ -fold larger photocurrent, along with the 3- and 2-fold faster oxidations of water and iodide, respectively, compared to the W-TNA samples. This enhancement was attributed to the creation of  $Ti(III)$  via oxygen vacancies, which was characterized in detail using various analytical tools. However, such a disordered surface was found to exhibit lower Faradaic efficiencies for multi-electron transferred oxidation reactions and higher Faradaic efficiencies for single-electron transfer oxidation reactions compared to W-TNAs. This suggests that B-TNAs can be used as photoanodes, both for driving the hydrogen evolution reaction on the counter electrode because of the large photocurrents and also for initiating value-added oxidation reactions via single-electron transfers.

## Acknowledgements

This research was supported by the Basic Science Research Program (2016R1A2B4007366) and the Space Core Technology Development Program (2014MA3A3A02034875) through the National Research Foundation, Korea. In addition, this work was partly supported by the Korea Ministry of Environment as Waste to Energy-Recycling Human Resource Development Project (YL-WE-17-001). We are grateful to the Korea CCS R&D Center (KCRC) (2014M1A8A1049354) and Korea Center for Artificial Photosynthesis (KCAP) (2009-0093880) for financial support. This publication was made possible by a grant from the Qatar National Research Fund under its National Priorities Research Program (NPRP 9-052-2-020).

## Appendix A. Supplementary data

Supplementary data associated with this article can be found, in the online version, at <https://doi.org/10.1016/j.apcatb.2017.12.043>.

## References

[1] S. Giménez, J. Bisquert, *Photoelectrochemical Solar Fuel Production*, Springer, 2016.

[2] U. Kang, S.K. Choi, D.J. Ham, S.M. Ji, W. Choi, D.S. Han, A. Abdel-Wahab, H. Park, Photosynthesis of formate from  $\text{CO}_2$  and water at 1% energy efficiency via copper iron oxide catalysis, *Energy Environ. Sci.* 8 (2015) 2638–2643.

[3] B.D. Sherman, J.J. Bergkamp, C.L. Brown, A.L. Moore, D. Gust, T.A. Moore, A tandem dye-sensitized photoelectrochemical cell for light driven hydrogen production, *Energy Environ. Sci.* 9 (2016) 1812–1817.

[4] T.H. Jeon, W. Choi, H. Park, Photoelectrochemical and photocatalytic behaviors of hematite-decorated titania nanotube arrays: energy level mismatch versus surface specific reactivity, *J. Phys. Chem. C* 115 (2011) 7134–7142.

[5] S.Y. Yang, W. Choi, H. Park,  $\text{TiO}_2$  nanotube array photoelectrocatalyst and  $\text{Ni-Sb-SnO}_2$  electrocatalyst bifacial electrodes: a new type of bifunctional hybrid platform for water treatment, *ACS Appl. Mater. Interfaces* 7 (2015) 1907–1914.

[6] M. Shang, H. Hu, G. Lu, Y. Bi, Synergistic effects of  $\text{SrTiO}_3$  nanocubes and  $\text{Ti}^{3+}$  dual-doping for highly improved photoelectrochemical performance of  $\text{TiO}_2$  nanotube arrays under visible light, *J. Mater. Chem. A* 4 (2016) 5849–5853.

[7] Q. Zhang, L. Wang, J. Feng, H. Xu, W. Yan, Enhanced photoelectrochemical performance by synthesizing  $\text{CdS}$  decorated reduced  $\text{TiO}_2$  nanotube arrays, *Phys. Chem. Chem. Phys.* 16 (2014) 23431–23439.

[8] J. Krysa, K. Lee, S. Pausova, S. Kment, Z. Hubicka, R. Ctvrtlik, P. Schmuki, Self-organized transparent 1D  $\text{TiO}_2$  nanotubular photoelectrodes grown by anodization of sputtered and evaporated Ti layers: a comparative photoelectrochemical study, *Chem. Eng. J.* 308 (2017) 745–753.

[9] D. Rafieian, W. Ogieglo, T. Savenije, R.G. Lammertink, Controlled formation of anatase and rutile  $\text{TiO}_2$  thin films by reactive magnetron sputtering, *AIP Adv.* 5 (2015) 097168.

[10] P. Shinde, S. Sadale, P. Patil, P. Bhosale, A. Brüger, M. Neumann-Spallart, C. Bhosale, Properties of spray deposited titanium dioxide thin films and their application in photoelectrocatalysis, *Sol. Energy Mater. Sol. Cells* 92 (2008) 283–290.

[11] W. Leng, P.R. Barnes, M. Juozapavicius, B.C. O'Regan, J.R. Durrant, Electron diffusion length in mesoporous nanocrystalline  $\text{TiO}_2$  photoelectrodes during water oxidation, *J. Phys. Chem. Lett.* 1 (2010) 967–972.

[12] A. Solbrand, A. Henningsson, S. Södergren, H. Lindström, A. Hagfeldt, S.-E. Lindquist, Charge transport properties in dye-sensitized nanostructured  $\text{TiO}_2$  thin film electrodes studied by photoinduced current transients, *J. Phys. Chem. B* 103 (1999) 1078–1083.

[13] A. Hagfeldt, U. Björkstén, S.-E. Lindquist, Photoelectrochemical studies of colloidal  $\text{TiO}_2$ -films: the charge separation process studied by means of action spectra in the UV region, *Sol. Energy Mater. Sol. Cells* 27 (1992) 293–304.

[14] Y.Y. Ahn, S.Y. Yang, C. Choi, W. Choi, S. Kim, H. Park, Electrocatalytic activities of  $\text{Sb-SnO}_2$  and  $\text{Bi-TiO}_2$  anodes for water treatment: effects of electrocatalyst composition and electrolyte, *Catal. Today* 282 (2017) 57–64.

[15] M. Yang, D. Kim, H. Jha, K. Lee, J. Paul, P. Schmuki, Nb doping of  $\text{TiO}_2$  nanotubes for an enhanced efficiency of dye-sensitized solar cells, *Chem. Commun.* 47 (2011) 2032–2034.

[16] U. Kang, H. Park, Lithium ion-inserted  $\text{TiO}_2$  nanotube array photoelectrocatalysts, *Appl. Catal. B* 140 (2013) 233–240.

[17] H. Pan, Y.-W. Zhang, V.B. Shenoy, H. Gao, Effects of H-N- and (H, N)-doping on the photocatalytic activity of  $\text{TiO}_2$ , *J. Phys. Chem. C* 115 (2011) 12224–12231.

[18] H. Li, Z. Chen, C.K. Tsang, Z. Li, X. Ran, C. Lee, B. Nie, L. Zheng, T. Hung, J. Lu, B. Pan, Y.Y. Li, Electrochemical doping of anatase  $\text{TiO}_2$  in organic electrolytes for high-performance supercapacitors and photocatalysts, *J. Mater. Chem. A* 2 (2014) 229–236.

[19] S. Li, J. Qiu, M. Ling, F. Peng, B. Wood, S. Zhang, Photoelectrochemical characterization of hydrogenated  $\text{TiO}_2$  nanotubes as photoanodes for sensing applications, *ACS Appl. Mater. Interfaces* 5 (2013) 11129–11135.

[20] A. Sinhamahapatra, J.-P. Jeon, J.-S. Yu, A new approach to prepare highly active and stable black titania for visible light-assisted hydrogen production, *Energy Environ. Sci.* 8 (2015) 3539–3544.

[21] K.-I. Li, Z.-b. Xie, S. Adams, A reliable  $\text{TiO}_2$  nanotube membrane transfer method and its application in photovoltaic devices, *Electrochim. Acta* 62 (2012) 116–123.

[22] Z. Chen, H.N. Dinh, E. Miller, *Photoelectrochemical Water Splitting: Standards, Experimental Methods, and Protocols*, Springer, New York, 2013.

[23] T.H. Jeon, A.D. Bokare, D.S. Han, A. Abdel-Wahab, H. Park, W. Choi, Dual modification of hematite photoanode by Sn-doping and  $\text{Nb}_2\text{O}_5$  layer for water oxidation, *Appl. Catal. B* 201 (2017) 591–599.

[24] Z. Lu, C.T. Yip, L. Wang, H. Huang, L. Zhou, Hydrogenated  $\text{TiO}_2$  nanotube arrays as high-rate anodes for lithium-ion microbatteries, *ChemPlusChem* 77 (2012) 991–1000.

[25] H.W. Jeong, W.-S. Chae, B. Song, C.-H. Cho, S.-H. Baek, Y. Park, H. Park, Optical resonance and charge transfer behavior of patterned  $\text{WO}_3$  microdisc arrays, *Energy Environ. Sci.* 9 (2016) 3143–3150.

[26] J. Kim, W.J.K. Choi, J. Choi, M.R. Hoffmann, H. Park, Electrolysis of urea and urine for solar hydrogen, *Catal. Today* 199 (2013) 2–7.

[27] N.C.D. Nath, S.Y. Choi, H.W. Jeong, J.-J. Lee, H. Park, Stand-alone photoconversion of carbon dioxide on copper oxide wire arrays powered by tungsten trioxide/dye-sensitized solar cell dual absorbers, *Nano Energy* 25 (2016) 51–59.

[28] S.Y. Choi, C.-D. Kim, D.S. Han, H. Park, Facilitating hole transfer on electrochemically synthesized p-type  $\text{CuAlO}_2$  films for efficient solar hydrogen production from water, *J. Mater. Chem. A* (2017).

[29] U. Kang, H. Park, A facile synthesis of  $\text{CuFeO}_2$  and  $\text{CuO}$  composite photocatalyst films for the production of liquid formate from  $\text{CO}_2$  and water over a month, *J. Mater. Chem. A* 5 (2017) 2123–2131.

[30] S.K. Choi, W.-S. Chae, B. Song, C.-H. Cho, J. Choi, D.S. Han, W. Choi, H. Park, Photoelectrochemical hydrogen production on silicon microwire arrays overlaid with ultrathin titanium nitride, *J. Mater. Chem. A* 4 (2016) 14008–14016.

[31] H. Zhou, Y. Zhang, Electrochemically self-doped  $\text{TiO}_2$  nanotube arrays for supercapacitors, *J. Phys. Chem. C* 118 (2014) 5626–5636.

[32] H. Wu, D. Li, X. Zhu, C. Yang, D. Liu, X. Chen, Y. Song, L. Lu, High-performance and renewable supercapacitors based on  $\text{TiO}_2$  nanotube array electrodes treated by an electrochemical doping approach, *Electrochim. Acta* 116 (2014) 129–136.

[33] I.S. Cho, J. Choi, K. Zhang, S.J. Kim, M.J. Jeong, L. Cai, T. Park, X. Zheng, J.H. Park, Highly efficient solar water splitting from transferred  $\text{TiO}_2$  nanotube arrays, *Nano Lett.* 15 (2015) 5709–5715.

[34] W. Liao, J. Yang, H. Zhou, M. Muruganathan, Y. Zhang, Electrochemically self-doped  $\text{TiO}_2$  nanotube arrays for efficient visible light photoelectrocatalytic degradation of contaminants, *Electrochim. Acta* 136 (2014) 310–317.

[35] G. Wang, H. Wang, Y. Ling, Y. Tang, X. Yang, R.C. Fitzmorris, C. Wang, J.Z. Zhang, Y. Li, Hydrogen-treated  $\text{TiO}_2$  nanowire arrays for photoelectrochemical water splitting, *Nano Lett.* 11 (2011) 3026–3033.

[36] H. Cui, W. Zhao, C. Yang, H. Yin, T. Lin, Y. Shan, Y. Xie, H. Gu, F. Huang, Black  $\text{TiO}_2$  nanotube arrays for high-efficiency photoelectrochemical water-splitting, *J. Mater. Chem. A* 2 (2014) 8612–8616.

[37] M.J. Elser, T. Berger, D. Brandhuber, J. Bernardi, O. Diwald, E. Knözinger, Particles coming together: electron centers in adjoined  $\text{TiO}_2$  nanocrystals, *J. Phys. Chem. B* 110 (2006) 7605–7608.

[38] T. Berger, M. Sterrer, O. Diwald, E. Knözinger, Charge trapping and photoadsorption of  $\text{O}_2$  on dehydroxylated  $\text{TiO}_2$  nanocrystals—an electron paramagnetic resonance study, *ChemPhysChem* 6 (2005) 2104–2112.

[39] A.L. Linsebigler, G. Lu, J.T. Yates, Photocatalysis on  $\text{TiO}_2$  surfaces: principles, mechanisms, and selected results, *Chem. Rev.* 95 (1995) 735–758.

[40] R. Kumar, S. Govindarajan, R.K. Siri Kiran Janardhana, T.N. Rao, S.V. Joshi, S. Anandan, Facile one-step route for the development of in situ cocatalyst-modified  $\text{Ti}^{3+}$  self-doped  $\text{TiO}_2$  for improved visible-light photocatalytic activity, *ACS Appl. Mater. Interfaces* 8 (2016) 27642–27653.

[41] C. Kim, S. Kim, J. Choi, J. Lee, J.S. Kang, Y.-E. Sung, J. Lee, W. Choi, J. Yoon, Blue  $\text{TiO}_2$  nanotube array as an oxidant generating novel anode material fabricated by simple cathodic polarization, *Electrochim. Acta* 141 (2014) 113–119.

[42] X. Lü, W. Yang, Z. Quan, T. Lin, L. Bai, L. Wang, F. Huang, Y. Zhao, Enhanced electron transport in Nb-doped  $\text{TiO}_2$  nanoparticles via pressure-induced phase transitions, *J. Am. Chem. Soc.* 136 (2014) 419–426.

[43] S. Anantharaj, P. Karthik, S. Kundu, Petal-like hierarchical array of ultrathin  $\text{Ni(OH)}_2$  nanosheets decorated with  $\text{Ni(OH)}_2$  nanoburls: a highly efficient OER electrocatalyst, *Catal. Sci. Technol.* 7 (2017) 882–893.

[44] Y.P. Zhu, T.Y. Ma, M. Jaroniec, S.Z. Qiao, Self-templating synthesis of hollow  $\text{Co}_3\text{O}_4$  microtube arrays for highly efficient water electrolysis, *Angew. Chem. Int. Ed.* 56 (2017) 1324–1328.

[45] D. Chandra, D. Takama, T. Masaki, T. Sato, N. Abe, T. Togashi, M. Kurihara, K. Saito, T. Yui, M. Yagi, Highly efficient electrocatalysis and mechanistic investigation of intermediate  $\text{IrO}_x(\text{OH})_y$  nanoparticle films for water oxidation, *ACS Catal.* 6 (2016) 3946–3954.

[46] J. Nowotny, T. Bak, M.K. Nowotny, L.R. Sheppard,  $\text{TiO}_2$  surface active sites for water splitting, *J. Phys. Chem. B* 110 (2006) 18492–18495.

[47] C.L. Muñich, Y. Zhou, A.M. Holder, A.W. Weimer, C.B. Musgrave, Effect of surface deposited Pt on the photoactivity of  $\text{TiO}_2$ , *J. Phys. Chem. C* 116 (2012) 10138–10149.

[48] S.Y. Yang, D. Kim, H. Park, Shift of the reactive species in the  $\text{Sb-SnO}_2$ -electrocatalyzed inactivation of *E. coli* and degradation of phenol: effects of nickel doping and electrolytes, *Environ. Sci. Technol.* 48 (2014) 2877–2884.

[49] S. Kim, S.K. Choi, B.Y. Yoon, S.K. Lim, H. Park, Effects of electrolyte on the electrocatalytic activities of  $\text{RuO}_2/\text{Ti}$  and  $\text{Sb-SnO}_2/\text{Ti}$  anodes for water treatment, *Appl. Catal. B* 97 (2010) 135–141.